Dynamics of the Electromagnetic Fields Induced by Fast Electron Propagation in Near-Solid-Density Media

L. Romagnani,[1,2,*] A. P. L. Robinson,[3] R. J. Clarke,[3] D. Doria,[4,2] L. Lancia,[1] W. Nazarov,[5] M. M. Notley,[3] A. Pipahl,[6] K. Quinn,[2] B. Ramakrishna,[7] P. A. Wilson,[8,9] J. Fuchs,[1] O. Willi,[6] and M. Borghesi[2]

[1]*LULI—CNRS, Ecole Polytechnique, CEA, Université Paris-Saclay, F-91128 Palaiseau cedex, France*
[2]*Centre for Plasma Physics, School of Mathematics and Physics, The Queen's University of Belfast, Belfast BT7 1NN, United Kingdom*
[3]*Central Laser Facility, Rutherford Appleton Laboratory, Chilton, OX11 0QX, United Kingdom*
[4]*Extreme Light Infrastructure—Nuclear Physics (ELI-NP), Horia Hulubei Institute for Nuclear Physics (IFIN-HH), Reactorului Str., 30, Magurele 077126, Bucharest, Romania*
[5]*School of Chemistry, University of St. Andrews, St Andrews KY16 9ST, United Kingdom*
[6]*Institut für Laser-und Plasmaphysik, Heinrich-Heine-Universität, Düsseldorf, 40225, Germany*
[7]*Department of Physics, Indian Institute of Technology Hyderabad 502285, India*
[8]*School of Engineering, University of South Australia, Adelaide SA 5095, Australia*
[9]*Department of Medical Physics, Royal Adelaide Hospital, Adelaide SA 5000, Australia*

(Received 8 June 2017; revised manuscript received 1 October 2018; published 14 January 2019)

The propagation of fast electron currents in near solid-density media was investigated via proton probing. Fast currents were generated inside dielectric foams via irradiation with a short (~0.6 ps) laser pulse focused at relativistic intensities ($I\lambda^2 \sim 4 \times 10^{19}$ W cm^{-2} μm^2). Proton probing provided a spatially and temporally resolved characterization of the evolution of the electromagnetic fields and of the associated net currents directly inside the target. The progressive growth of beam filamentation was temporally resolved and information on the divergence of the fast electron beam was obtained. Hybrid simulations of electron propagation in dense media indicate that resistive effects provide a major contribution to field generation and explain well the topology, magnitude, and temporal growth of the fields observed in the experiment. Estimations of the growth rates for different types of instabilities pinpoints the resistive instability as the most likely dominant mechanism of beam filamentation.

DOI: 10.1103/PhysRevLett.122.025001

The propagation of laser-generated fast electron currents in dense plasmas is a fundamental topic in laser-plasma investigations and is of crucial interest for a number of applications, including the fast ignition (FI) approach to inertial confinement fusion (ICF) (see Refs. [1,2] and references therein) and the generation of secondary radiation or particle beams, e.g., x- and γ-ray radiation [3–6] or positron [7–9] and ion beams [10–12]. The extreme current densities involved in intense laser-plasma interactions mean that fast electron transport cannot be merely reduced to ballistic propagation with collisional effects [13–16]. It is now widely accepted that self-consistently generated electromagnetic fields play a critical role, leading to electric inhibition [17–22] or magnetic pinching and filamentation [23–27], amongst other effects [28–31]. The growth of these fields can be highly dependent on the background resistivity [13–16], which means that a reliable modeling of the electrical properties of the propagation medium is required. Although a number of different theoretical and computational approaches can be found in the literature [32–43], experimental testing of these models is difficult and is open to questions of interpretation and analysis. Experimental investigations typically rely on measurements of K_α emission from high-Z targets [30,31] or buried layers [17–21], on (somewhat qualitative) optical probing through transparent media [22–25], on the spatial and/or spectral characterization of the fraction of electrons that escape the target [26,27], or on measurements of radiation emission at the target-vacuum interface [22,27–29]. While these techniques provide valuable data, more direct information would be obtained if one could map and temporally resolve the evolution of the self-generated electromagnetic fields and related currents inside the target.

In this Letter we present the results of such an investigation effort. In the experiment fast electron currents were generated inside dielectric foams via intense and short-pulse laser irradiation. The electromagnetic fields accompanying fast electron propagation were spatially and temporally characterized directly inside the near solid-density and optically opaque target by using a laser-accelerated proton beam as a charged particle probe [44–55]. The distribution of the fields, and of the associated net currents, was quantitatively reconstructed via direct

deconvolution of the experimental proton images [47–52] and via comparison with particle tracing simulations [53–55]. Notably the growth of a filamentation instability was temporally resolved and information on the electron beam divergence was obtained for our experimental conditions. Three-dimensional (3D) hybrid simulations of electron propagation in dense media [41–43], carried out over spatial and temporal scales comparable to the experimental ones, suggest that resistive effects provide a major contribution to field generation. Comparison of the experimentally measured filamentation growth rates with analytical estimations for different instabilities identifies the resistive instability as the most likely dominant mechanism of beam filamentation.

The experiment was carried out at the Rutherford Appleton Laboratory (RAL), employing the petawatt (PW) beam line of the Vulcan laser system operating in the optical parametric chirped pulse amplification mode (OPCPA). The main PW beam (wavelength ~1.06 μm, pulse duration ~0.6 ps) was split into two separate beams $OPCPA_1$ and $OPCPA_2$. A sketch of the beams' focusing and targets' arrangements is shown in Fig. 1(a). $OPCPA_1$ (energy ~15–20 J, intensity $\sim 3.5 \times 10^{19}$ W cm^{-2}) was focused onto dielectric foam targets to induce a fast electron current in the target bulk. $OPCPA_2$ (energy ~240–340 J, intensity $\sim 10^{20}$ W cm^{-2}) was focused onto 25 μm thick gold foils to accelerate a broad energy spectrum proton beam (PB) (with typical maximum energies ~30 MeV) via target normal sheath acceleration (TNSA). The proton beam was used as a charged particle probe in a point-projection imaging, differential time-of-flight arrangement to map the electromagnetic fields generated inside the foams [44–46,49]. A multilayer stack of radiochromic films (RCFs) was used as particle detector [44–46,49]. The spectral selection properties of the RCF stack, coupled with the broad spectral content of the TNSA beam and with the differential time-of-flight arrangement, provided intrinsic temporal multiframe capabilities within a single laser shot [44,46,49].

Trimethylolpropane triacrylate (TMPTA, chemical formula $C_{15}H_{20}O_6$) foams with densities ranging from 20 mg cc^{-1} to 200 mg cc^{-1} and made of pure TMPTA or doped with different percentages of Br or Cl were tested to find the best observational conditions, which corresponded to the midrange density (50 mg cc^{-1} to 100 mg cc^{-1}) undoped foams. Each foam consisted of a 300 μm thick, (1.5–2) mm diameter half-disk. The irradiated foam surface was covered with a ~75 nm thick gold coating to avoid transparency to the laser light prior to ionization. The advantage of using foam targets is multifold. First, given the large resistivity expected in dielectric materials, plastic foams are ideal candidates to investigate the generation of resistive fields [27]. Second, in comparison with solid density materials, the use of foams reduces the integrated areal density seen by the protons probing through the target, hence limiting the loss of spatial resolution due to random multiple scattering by the target material. This is a crucial requirement in order to be able to observe fine structures, such as for instance those resulting from filamentation of the electron currents. To further reduce scattering effects we maximized the proton energies by using the higher intensity beam $OPCPA_2$ for proton acceleration. Meanwhile, irradiating the foam with the lower intensity beam $OPCPA_1$ limited contamination of the RCFs by spurious radiation and particles emitted from the foam.

Typical proton images and proton density lineouts of a laser-irradiated foam are shown in Figs. 1(b)–1(f). In the proton images zones with a darker (lighter) color correspond to regions of accumulation (depletion) of the probing protons, and proton density modulations $\delta n_p/n_{p0}$ (where $\delta n_p = n_p - n_{p0}$, with n_p and n_{p0} being the modulated and

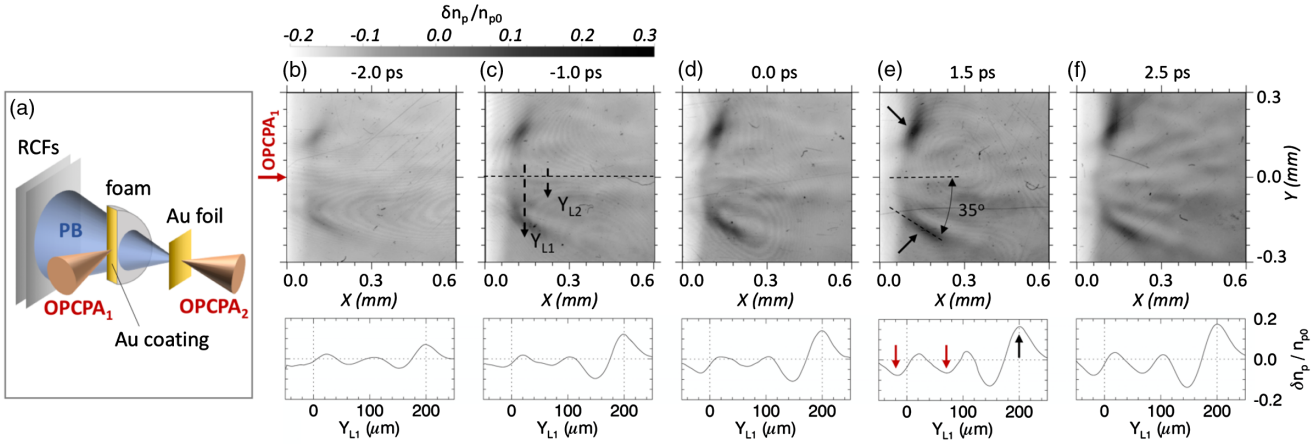

FIG. 1. (a) Sketch of the targets' and beams' arrangement. (b)–(f) Typical experimental proton images of an irradiated 100 mg cc^{-1} undoped TMPTA foam and corresponding proton density modulation lineouts along Y_{L1}. All temporal frames were acquired in the same laser shot and probing times refer to the peak of the $OPCPA_1$ laser pulse. In (e) black arrows indicate the lateral lobes of proton accumulation and red arrows indicate the modulations associated with beam filamentation.

the background proton densities, respectively) reflect modulations in the amplitudes of the electromagnetic fields associated with the propagation of currents in the foam (see Refs. [47,51,52] and analysis below). The evolution of the main features observed in the proton images is as follows. Upon laser irradiation, two lobes of increased proton density diverging from the laser focal spot position are observed to form [Figs. 1(b)–1(f), indicated by black arrows in 1(e)]. The two lobes begin to form typically few picoseconds before the peak of the laser pulse, indicating that electron injection is already initiated by the raising edge of the pulse. At later probing times, filamented structures are observed to develop within the region delimited by the two lateral lobes [Figs. 1(b)–1(f), indicated by red arrows in (e)]. The amplitudes of the proton density modulations are observed to grow in time, eventually reaching maximum values over ∼ picosecond(s) timescales.

For our target and irradiation parameters, it is expected that the injection of fast electrons into the target by the laser pulse will be balanced by the generation of a resistive return current [13,14,16–29]. To model these conditions, simulations were performed with the hybrid code ZEPHYROS [42,43], largely based on the methods established by Davies [14,16]. The code treats fast electrons with particle-in-cell methods and the background plasma with a fluid approach, modeling resistive field generation [$\mathbf{E} = \eta \mathbf{j}_r$, $\partial \mathbf{B}/\partial t = -\nabla \times (\eta \mathbf{j}_r)$] and drag or scattering of the fast electrons by the background [41]. Specific heat capacity and ionization of the background are described within a Thomas-Fermi model, while the local resistivity is calculated according to a model based on that of Lee and More [56]. Notably, the use of an hybrid code allowed performing 3D simulations over spatial and temporal scales comparable to the experimental ones and at target densities matching the experiment. In the simulations the background mass density was chosen equal to the foam density of 100 mg cc^{-1}. Electron injection modeled electron acceleration from a laser beam with a FWHM focal spot radius of 5 μm, an intensity of 3.5×10^{19} W cm^{-2} and a pulse duration of 0.6 ps. The fast electron energy distribution was taken to be exponential, with an electron temperature $k_B T_e \sim 2$ MeV as given by ponderomotive scaling [57,58]. A fast electron current $j_{e0} \sim 4.5 \times 10^{16}$ A m^{-2} at the injection point was estimated from energy conservation, assuming a laser to fast electron conversion efficiency of 30%. Several runs were performed varying the beam angular distribution (top-flat, Gaussian, and Airy distributions with different divergence angles were tested).

In the simulations, the fast electron current $\mathbf{j}_e$ is observed to propagate as a conical beam diverging from the injection point, driving a return current $\mathbf{j}_r \simeq -\mathbf{j}_e$. Electron propagation is accompanied by the fast growth of large amplitude electric and magnetic fields via a resistive mechanism. An electric field directed along the direction of the return

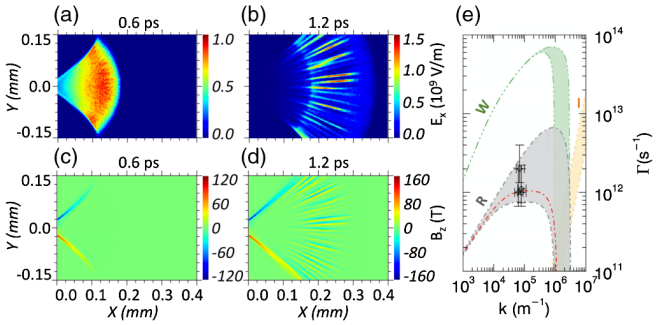

FIG. 2. [(a), (b)] electric field E_x and [(c), (d)] magnetic field B_z distributions from ZEPHYROS simulations. In [(c), (d)] red (blue) color indicates a field exiting (entering) the page and normal to it. (e) Theoretical growth rates for the resistivity (R) and Weibel (W) instabilities (for 0.02 MeV $\leq T_\perp \leq$ 0.2 MeV) and for the ionization (I) instability (for background ionization potentials 5 eV $\leq I_a \leq$ 15 eV). Scatter points $(k, \Gamma) = (2\pi/\lambda_f, 1/\tau_f)$ are the filamentation growth rates inferred from the experimental data and the red dash-dot line is their best R fit (corresponding to $T_\perp \sim 0.15$ MeV).

current flow fills the whole conical beam [Figs. 2(a) and 2(b)], while an azimuthal magnetic field looping around the beam grows at the edge of the cone [Figs. 2(c) and 2(d)]. Both field distributions exhibit smooth gradients in the direction of the current flow due to the longitudinal spreading of the beam, while they have sharp descending gradients in the transverse direction at the edge of the beam. At the later simulation times the beam undergoes filamentation [Figs. 2(b) and 2(d)]. Each filament is characterized by a transverse (with respect to the local current direction) modulation of the electric field amplitude and by a magnetic field looping around the filament. We verified that varying the injected beam parameters within the experimental uncertainties, or choosing different beam angular distributions, does not change the order of magnitude and main topology of the fields. We also verified that the inclusion of magnetic field generation via Biermann battery only provides a minor contribution (few %) in comparison to the resistive mechanism.

Based on the simulation results we can infer that the electric field is expected to be directed mainly along the current flow direction (see also Refs. [35,40]), and should not contribute significantly to the transverse modulations observed in the experiment. These can therefore be mainly related to particle deflections by the magnetic field. On this ground, following Refs. [47,51,52], we have $\delta n_p/n_{p0} \simeq -(eL/2\mathcal{E}_p M)\nabla_{\perp 0} \cdot \int (\mathbf{v_p} \times \mathbf{B})_\perp dz$ (where e is the elementary charge, L the foam to RCF distance, $\mathcal{E}_p$ the proton energy, M the projection magnification, and $\mathbf{v_p}$ the proton velocity). The magnetic field and net current distributions in one of the lateral lobes and in a filament, as approximatively reconstructed from the RCF lineouts using this relation, are shown in Figs. 3(a)–3(d). Inspection of Figs. 3(a) and 3(b) shows that the lateral lobes observed in

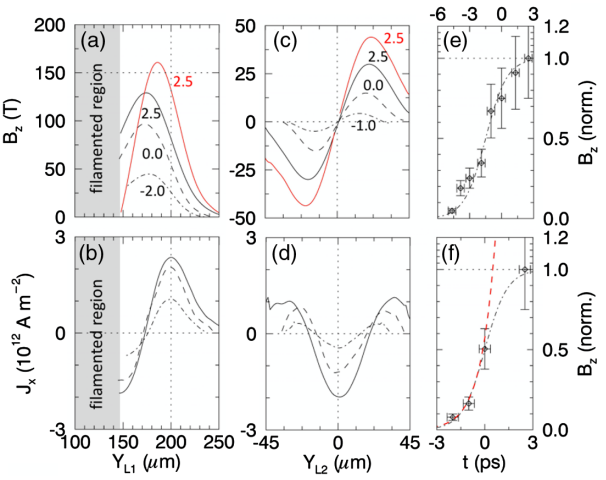

FIG. 3. Magnetic field B_z and net current density J_x for three probing times (in ps over the plots), [(a), (b)] in one of the lateral lobes and [(c), (d)] in a filament. Spatially averaged quantities are in black and Abel-inverted profiles in red. Normalized peak magnetic fields versus probing time (e) for the lateral lobe and (f) for the filament. Scatter points are the experimental data, black dash-dot lines are fits with logistic functions and the red dash line in (f) is an exponential fit $\propto e^{t/\tau_f}$.

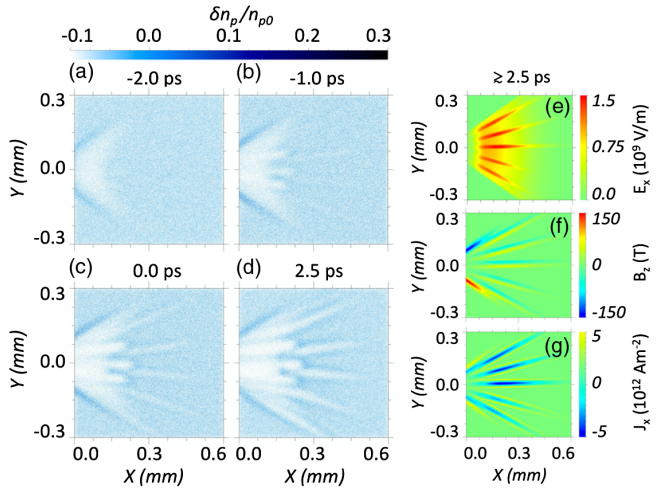

FIG. 4. (a)–(d) Synthetic proton images from qTrace simulations. Slice maps of (e) the electric E_x, (f) the magnetic field B_z and (g) the net current density J_x at saturation. In (f) red (blue) color indicates a field exiting (entering) the page and normal to it.

the proton images are associated with a magnetic field peaked at the edge of the electron beam, where a nonzero net current develops as a result of a local imbalance between the fast and return currents. Similar field and current distributions are also found in the filaments [Figs. 3(c) and 3(d)]. Both in the lateral lobes and in the filaments the field initially grows exponentially, until it eventually reaches a saturation level [Figs. 3(e) and 3(f)]. Specifically, in the filaments typical growth times $\tau_f \sim (0.5\text{–}1)$ ps are found for filamentation wavelengths $\lambda_f \sim (50\text{–}100)$ μm.

To move beyond the approximations used in the deconvolution of the proton density lineouts, and to obtain global maps of the electromagnetic fields and net currents, we compared the experimental proton density modulations with those obtained from particle tracing simulations (PTs) carried out with the 3D code qTrace [47]. In PTs the deflections of protons when crossing a time-dependent field distribution, reproducing the main topology and temporal evolution of the fields from ZEPHYROS simulations, were computed numerically to generate synthetic proton images [47,52,55]. Proton scattering by the foam material was additionally modeled via an extended Highland formula [59–61]. Detailed matching between the synthetic [Figs. 4(a)–4(d)] and experimental proton images was found for peak magnetic fields at saturation of $\sim$(140–160) T in the lateral lobes and of $\sim$(20–60) T in the filaments [Fig. 4(f); see Fig. 4(g) for the corresponding net current density]. PTs confirm that the modulations observed in the proton images are mainly determined by the magnetic field, while the electric field [shown in Fig. 4(e)] gives only a minor contribution. Specifically, the magnetic field delimiting the electron beam accumulates the probe protons at the edge of the beam image, producing the observed lateral lobes. The lobes' angular separation $\sim$(35°–45°) thus provides an estimation of the beam divergence [see Fig. 1(e)].

We further investigated the mechanism responsible for the beam filamentation observed in the experiment. Resistivity [32,62,63], ionization [63,64], and Weibel [65–67] instabilities are typically invoked to explain the filamentation of fast currents observed experimentally [23–27]. In physical terms resistive filamentation occurs because any transverse perturbation in the current density will resistively grow a magnetic field that drives fast electrons into the perturbation. As this increases the local current density, a positive feedback is created. The growth rate Γ for resistive filamentation (including magnetic field diffusion and thermal effects) can be described by a cubic dispersion relation $\Gamma^3 + a\Gamma^2 + b\Gamma + c = 0$, where $a = k^2\eta/\mu_0$, $b = k^2 T_\perp/\gamma_e m_e$ and $c = (k^4\eta T_\perp/\mu_0\gamma_e m_e) - (k^2 j_e^2\eta/\gamma m_e n_e)$ [32,62]. Here k is the transverse wave number of the instability, η is the background resistivity, and the fast electron beam is characterized by a current density j_e, electron density n_e, Lorentz factor γ_e, and transverse temperature $T_\perp$ (in eV). In our case, from geometrical considerations and comparison with the hybrid simulations, we can estimate at the filaments' location $n_e \sim 10^{19}$ cm^{-3}, $j_e \sim 5 \times 10^{14}$ A m^{-2}, $\gamma_e \sim 5$, $T_\perp \sim (0.01\text{–}0.1)T_e \sim (0.02\text{–}0.2)$ MeV and $\eta \sim 10^{-6}$ Ω m. Correspondingly, the maximum growth rates occur for instability wavelengths $\lambda_{\rm res} = 2\pi/k \sim (5\text{–}70)$ μm with growth times $\tau_{\rm res} \sim (0.15\text{–}1.3)$ ps [Fig. 2(e)], which compares well with the experimentally measured filaments' size and growth times. By contrast a similar estimation predicts

wavelengths $\lambda_{\mathrm{Weibel}} \sim (5\text{–}15)$ μm with faster growth times $\tau_{\mathrm{Weibel}} \sim 15$ fs for the Weibel mode [66,67], while for growth rates comparable to our observations smaller $\sim\mu$m size filaments are predicted for the ionization instability [29,63,64]. In a likely scenario the Weibel and ionization instabilities may provide an initial seed for the beam filamentation, until eventually the resistive mode becomes the dominant mechanism.

In conclusion we obtained a detailed experimental characterization of the electromagnetic fields and of the net currents associated with fast electron propagation in near solid-density media. Comparisons with hybrid simulations and estimations of instability growth rates indicate that, for our experimental conditions, resistive effects are likely to provide a major contribution to field generation and beam filamentation. Our results should be stimulating for further investigations and provide valuable data for comparison with existing theoretical and computational models.

The authors acknowledge the support of EPSRC (Grants No. EP/C003586/1, No. EP/K022415/1), the STFC Direct Access scheme, the British Council, the studentship support from AWE plc and ANDOR Technology and the DFG SFB/TR18 and GRK1203 programs.

*lorenzo.romagnani@polytechnique.edu

[1] R. S. Craxton, K. S. Anderson, T. R. Boehly, V. N. Goncharov, D. R. Harding, J. P. Knauer, R. L. McCrory, P. W. McKenty, D. D. Meyerhofer, J. F. Myatt *et al.*, Phys. Plasmas **22**, 110501 (2015).
[2] R. Betti and O. A. Hurricane, Nat. Phys. **12**, 435 (2016).
[3] C. Gahn, G. Pretzler, A. Saemann, G. D. Tsakiris, K. J. Witte, D. Gassmann, T. Schätz, U. Schramm, P. Thirolf, and D. Habs, Appl. Phys. Lett. **73**, 3662 (1998).
[4] J. Yu, Z. Jiang, J. C. Kieffer, and A. Krol, Phys. Plasmas **6**, 1318 (1999).
[5] P. A. Norreys, M. Santala, E. Clark, M. Zepf, I. Watts, F. N. Beg, K. Krushelnick, M. Tatarakis, A. E. Dangor, X. Fang *et al.*, Phys. Plasmas **6**, 2150 (1999).
[6] K. W. D. Ledingham, I. Spencer, T. McCanny, R. P. Singhal, M. I. K. Santala, E. Clark, I. Watts, F. N. Beg, M. Zepf, K. Krushelnick *et al.*, Phys. Rev. Lett. **84**, 899 (2000).
[7] T. E. Cowan, M. D. Perry, M. H. Key, T. R. Ditmire, S. P. Hatchett, E. A. Henry, J. D. Moody, M. J. Moran, D. M. Pennington, T. W. Phillips *et al.*, Laser Part. Beams **17**, 773 (1999).
[8] C. Gahn, G. D. Tsakiris, G. Pretzler, K. J. Witte, C. Delfin, C.-G. Wahlström, and D. Habs, Appl. Phys. Lett. **77**, 2662 (2000).
[9] H. Chen, S. C. Wilks, J. D. Bonlie, E. P. Liang, J. Myatt, D. F. Price, D. D. Meyerhofer, and P. Beiersdorfer, Phys. Rev. Lett. **102**, 105001 (2009).
[10] E. L. Clark, K. Krushelnick, J. R. Davies, M. Zepf, M. Tatarakis, F. N. Beg, A. Machacek, P. A. Norreys, M. I. K. Santala, I. Watts, and A. E. Dangor, Phys. Rev. Lett. **84**, 670 (2000).
[11] A. Maksimchuk, S. Gu, K. Flippo, D. Umstadter, and V. Yu. Bychenkov, Phys. Rev. Lett. **84**, 4108 (2000).
[12] R. A. Snavely, M. H. Key, S. P. Hatchett, T. E. Cowan, M. Roth, T. W. Phillips, M. A. Stoyer, E. A. Henry, T. C. Sangster, M. S. Singh *et al.*, Phys. Rev. Lett. **85**, 2945 (2000).
[13] A. R. Bell, J. R. Davies, S. Guerin, and H. Ruhl, Plasma Phys. Controlled Fusion **39**, 653 (1997).
[14] J. R. Davies, A. R. Bell, M. G. Haines, and S. M. Guérin, Phys. Rev. E **56**, 7193 (1997).
[15] J. R. Davies, Phys. Rev. E **65**, 026407 (2002).
[16] J. R. Davies, Phys. Rev. E **68**, 056404 (2003).
[17] M. H. Key, M. D. Cable, T. E. Cowan, K. G. Estabrook, B. A. Hammel, S. P. Hatchett, E. A. Henry, D. E. Hinkel, J. D. Kilkenny, J. A. Koch *et al.*, Phys. Plasmas **5**, 1966 (1998).
[18] K. B. Wharton, S. P. Hatchett, S. C. Wilks, M. H. Key, J. D. Moody, V. Yanovsky, A. A. Offenberger, B. A. Hammel, M. D. Perry, and C. Joshi, Phys. Rev. Lett. **81**, 822 (1998).
[19] D. Batani, J. R. Davies, A. Bernardinello, F. Pisani, M. Koenig, T. A. Hall, S. Ellwi, P. Norreys, S. Rose, A. Djaoui, and D. Neely, Phys. Rev. E **61**, 5725 (2000).
[20] F. Pisani, A. Bernardinello, D. Batani, A. Antonicci, E. Martinolli, M. Koenig, L. Gremillet, F. Amiranoff, S. Baton, J. Davies *et al.*, Phys. Rev. E **62**, R5927 (2000).
[21] D. Batani, A. Antonicci, F. Pisani, T. A. Hall, D. Scott, F. Amiranoff, M. Koenig, L. Gremillet, S. Baton, E. Martinolli, C. Rousseaux, and W. Nazarov, Phys. Rev. E **65**, 066409 (2002).
[22] D. Batani, S. D. Baton, M. Manclossi, J. J. Santos, F. Amiranoff, M. Koenig, E. Martinolli, A. Antonicci, C. Rousseaux, M. Rabec Le Gloahec *et al.*, Phys. Rev. Lett. **94**, 055004 (2005).
[23] M. Borghesi, A. J. Mackinnon, A. R. Bell, G. Malka, C. Vickers, O. Willi, J. R. Davies, A. Pukhov, and J. Meyer-ter-Vehn, Phys. Rev. Lett. **83**, 4309 (1999).
[24] L. Gremillet, F. Amiranoff, S. D. Baton, J.-C. Gauthier, M. Koenig, E. Martinolli, F. Pisani, G. Bonnaud, C. Lebourg, C. Rousseaux *et al.*, Phys. Rev. Lett. **83**, 5015 (1999).
[25] M. Tatarakis, F. N. Beg, E. L. Clark, A. E. Dangor, R. D. Edwards, R. G. Evans, T. J. Goldsack, K. W. D. Ledingham, P. A. Norreys, M. A. Sinclair, M-S. Wei, M. Zepf, and K. Krushelnick, Phys. Rev. Lett. **90**, 175001 (2003).
[26] M. S. Wei, F. N. Beg, E. L. Clark, A. E. Dangor, R. G. Evans, A. Gopal, K. W. D. Ledingham, P. McKenna, P. A. Norreys, M. Tatarakis, M. Zepf, and K. Krushelnick, Phys. Rev. E **70**, 056412 (2004).
[27] R. Jung, J. Osterholz, K. Löwenbrück, S. Kiselev, G. Pretzler, A. Pukhov, O. Willi, S. Kar, M. Borghesi, W. Nazarov, S. Karsch, R. Clarke, and D. Neely, Phys. Rev. Lett. **94**, 195001 (2005).
[28] J. J. Santos, F. Amiranoff, S. D. Baton, L. Gremillet, M. Koenig, E. Martinolli, M. Rabec Le Gloahec, C. Rousseaux, D. Batani, A. Bernardinello, G. Greison, and T. Hall, Phys. Rev. Lett. **89**, 025001 (2002).
[29] M. Manclossi, J. J. Santos, D. Batani, J. Faure, A. Debayle, V. T. Tikhonchuk, and V. Malka, Phys. Rev. Lett. **96**, 125002 (2006).

[30] K. L. Lancaster, J. S. Green, D. S. Hey, K. U. Akli, J. R. Davies, R. J. Clarke, R. R. Freeman, H. Habara, M. H. Key, R. Kodama *et al.*, Phys. Rev. Lett. **98**, 125002 (2007).
[31] J. S. Green, V. M. Ovchinnikov, R. G. Evans, K. U. Akli, H. Azechi, F. N. Beg, C. Bellei, R. R. Freeman, H. Habara, R. Heathcote *et al.*, Phys. Rev. Lett. **100**, 015003 (2008).
[32] L. Gremillet, G. Bonnaud, and F. Amiranoff, Phys. Plasmas **9**, 941 (2002).
[33] J. J. Honrubia, A. Antonicci, and D. Moreno, Laser Part. Beams **22**, 129 (2004).
[34] R. J. Mason, E. S. Dodd, and B. J. Albright, Phys. Rev. E **72**, 015401 (2005).
[35] R. G. Evans, High Energy Density Phys. **2**, 35 (2006).
[36] Y. Sentoku and A. J. Kemp, J. Comput. Phys. **227**, 6846 (2008).
[37] B. I. Cohen, A. J. Kemp, and L. Divol, J. Comput. Phys. **229**, 4591 (2010).
[38] R. J. Kingham, M. Sherlock, C. P. Ridgers, and R. G. Evans, J. Phys.: Conf. Ser. **244**, 022042 (2010).
[39] H. Schmitz, R. Lloyd, and R. G. Evans, Plasma Phys. Controlled Fusion **54**, 085016 (2012).
[40] A. Héron and J. C. Adam, Phys. Plasmas **22**, 072306 (2015).
[41] A. P. L. Robinson, D. J. Strozzi, J. R. Davies, L. Gremillet, J. J. Honrubia, T. Johzaki, R. J. Kingham, M. Sherlock, and A. A. Solodov, Nucl. Fusion **54**, 054003 (2014).
[42] A. P. L. Robinson, H. Schmitz, J. S. Green, C. P. Ridgers, N. Booth, and J. Pasley, Phys. Plasmas **22**, 043118 (2015).
[43] A. P. L. Robinson and H. Schmitz, Phys. Plasmas **22**, 103104 (2015).
[44] M. Borghesi, A. Schiavi, D. H. Campbell, M. G. Haines, O. Willi, A. J. MacKinnon, L. A. Gizzi, M. Galimberti, R. J. Clarke, and H. Ruhl, Plasma Phys. Controlled Fusion **43**, A267 (2001).
[45] A. J. Mackinnon, P. K. Patel, R. P. Town, M. J. Edwards, T. Phillips, S. C. Lerner, D. W. Price, D. Hicks, M. H. key, S. Hatchett *et al.*, Rev. Sci. Instrum. **75**, 3531 (2004).
[46] L. Romagnani, M. Borghesi, C. A. Cecchetti, S. Kar, P. Antici, P. Audebert, S. Bandhoupadjay, F. Ceccherini, T. Cowan, J. Fuchs *et al.*, Laser Part. Beams **26**, 241 (2008).
[47] L. Romagnani, Ph.D. Thesis, The Queen's University Belfast, Belfast, United Kingdom, 2005.
[48] M. Borghesi, S. Bulanov, D. H. Campbell, R. J. Clarke, T. Zh Esirkepov, M. Galimberti, L. A. Gizzi, A. J. Mackinnon, N. M. Naumova, F. Pegoraro, H. Ruhl, A. Schiavi, and O. Willi, Phys. Rev. Lett. **88**, 135002 (2002).
[49] L. Romagnani, S. V. Bulanov, M. Borghesi, P. Audebert, J. C. Gauthier, K. Löwenbruck, A. J. Mackinnon, P. Patel, G. Pretzler, T. Toncian, and O. Willi, Phys. Rev. Lett. **101**, 025004 (2008).
[50] G. Sarri, C. A. Cecchetti, L. Romagnani, C. M. Brown, D. J. Hoarty, S. James, J. Morton, M. E. Dieckmann, R. Jung, O. Willi, S. V. Bulanov, F. Pegoraro, and M. Borghesi, New J. Phys. **12**, 045006 (2010).
[51] N. Kugland, D. D. Ryutov, C. Plechaty, J. S. Ross, and H.-S. Park, Rev. Sci. Instrum. **83**, 101301 (2012).
[52] C. Graziani, P. Tzeferacos, D. Q. Lamb, and C. Li, Rev. Sci. Instrum. **88**, 123507 (2017).
[53] L. Romagnani, J. Fuchs, M. Borghesi, P. Antici, P. Audebert, F. Ceccherini, T. Cowan, T. Grismayer, S. Kar, A. Macchi, P. Mora, G. Pretzler, A. Schiavi, T. Toncian, and O. Willi, Phys. Rev. Lett. **95**, 195001 (2005).
[54] L. Romagnani, A. Bigongiari, S. Kar, S. V. Bulanov, C. A. Cecchetti, T. Zh. Esirkepov, M. Galimberti, R. Jung, T. V. Liseykina, A. Macchi, J. Osterholz, F. Pegoraro, O. Willi, and M. Borghesi, Phys. Rev. Lett. **105**, 175002 (2010).
[55] M. C. Levy, D. D. Ryutov, S. C. Wilks, J. S. Ross, C. M. Huntington, F. Fiuza, D. A. Martinez, N. L. Kugland, M. G. Baring, and H.-S. Park, Rev. Sci. Instrum. **86**, 033302 (2015).
[56] Y. T. Lee and R. M. More, Phys. Fluids **27**, 1273 (1984).
[57] S. C. Wilks, W. L. Kruer, M. Tabak, and A. B. Langdon, Phys. Rev. Lett. **69**, 1383 (1992).
[58] S. C. Wilks and W. L. Kruer, IEEE J. Quantum Electron. **33**, 1954 (1997).
[59] V. L. Highland, Nucl. Instrum. Methods **129**, 497 (1975); **161**, 171 (1979).
[60] N. Kanematsu, Nucl. Instrum. Methods Phys. Res., Sect. B **266**, 5056 (2008).
[61] N. Kanematsu, Phys. Med. Biol. **54**, N67 (2009).
[62] A. P. L. Robinson, R. J. Kingham, C. P. Ridgers, and M. Sherlock, Plasma Phys. Controlled Fusion, **50**, 065019 (2008).
[63] A. Debayle and V. T. Tikhonchuk, Phys. Rev. E **78**, 066404 (2008).
[64] S. I. Krasheninnikov, A. V. Kim, B. K. Frolov, and R. Stephens, Phys. Plasmas **12**, 073105 (2005).
[65] E. S. Weibel, Phys. Rev. Lett. **2**, 83 (1959).
[66] B. D. Fried, Phys. Fluids **2**, 337 (1959).
[67] A. Grassi, M. Grech, F. Amiranoff, F. Pegoraro, A. Macchi, and C. Riconda, Phys. Rev. E **95**, 023203 (2017).